Comparison of mixing processes in a compressible accelerated nozzle flow with subsonic and supersonic injection

Anja Wohler⋆*, Khadijeh Mohri*⋆⋆*, Christof Schulz*⋆⋆ *and Bernhard Weigand*⋆
⋆*Institut für Thermodynamik der Luft- und Raumfahrt (ITLR), Universität Stuttgart*
Pfaffenwaldring 31, 70569 Stuttgart, Germany
⋆⋆*Institut für Verbrennung und Gasdynamik (IVG), Universität Duisburg-Essen*
Lotharstr. 1, 47057 Duisburg, Germany

Abstract

The mixing behaviour of a gaseous injector flow in a compressible accelerated nozzle flow was investigated. To visualize the flow structures laser-induced fluorescence (LIF) imaging was applied. These flow structures were shown for four different injectors with their trailing edge in the supersonic part of the flow and compared to four injectors with their trailing edge in the subsonic region. Instantaneous images showed the zig-zag like flow structures and the recompression region behind the injectors in case of supersonic injection. The half-width of the growing wake was calculated and this followed the 1/2-power-law. The intensity at the centerline decreased asymptotically and the wake showed a self-preserving state.

1. Introduction

Mixing of gases in high-enthalpy flows is important in many engineering applications. In this study mixing processes in a compressible accelerated nozzle flow were investigated within the framework of a research activity devoted to the development of strategies for gasdynamically-induced nanoparticle synthesis [1, 2]. Here, nanoparticles are produced from gas-phase precursors in a shock-wave flow reactor. Due to the high velocity and short mixing time, efficient and rapid mixing is necessary and a spatially and temporally homogeneous mixture of the injected evaporated precursor with the ambient air is required to achieve high quality nanoparticles with a narrow size distribution. Therefore, the mixing was investigated from the end of the injector trailing edge to the shock train that initiate the chemical reaction which lead to the generation and growth of the nanoparticles. Also in combustion processes when rapid fuel and air mixing is desired, large entrainment rates of oxidizer into the injected fuel stream are required. Because of the importance of these mixing processes extensive research has been done in the past. It is shown that large-scale two-dimensional coherent structures, observed in incompressible planar shear layers, play an important role in entrainment and mixing processes [3]. Furthermore, lobed mixers were investigated and an enhancement in mixing due to streamwise vortices in incompressible flows is shown [4]. In addition, the universality of the wake structures' self-preserving state caused by different wake generators (e.g., circular cylinders, a symmetrical airfoil, and a flat plate) is proven for incompressible wakes [5]. It is shown that the normalized characteristic velocity and the length scales depend on the initial conditions but it is shown also that the normalized mean velocity profile is independent from the initial conditions and the shape of the wake generator. In wakes at higher Mach numbers compressibility effects impact the structures strongly [6, 7]. Furthermore, the spreading rate of the mixing layer decreases with increasing Mach number [8]. In confined, supersonic, planar, turbulent, bluff-body wakes at various Mach numbers, the normalized mean velocity profiles are invariant at different downstream locations and in good agreement with the incompressible wakes profile [9]. Further research has been done for RAMJET and SCRAMJET engines [10, 11]. For the use in SCRAMJET engines lobed injector geometries are known for the generation of large-scale streamwise vortices and thus to improve mixing [12, 13].

So far, no attention has been dedicated to mixing processes in compressible, accelerated nozzle flows with blunt-body wakes. In the case of the nanoparticle synthesis reactor, the wake starts in the subsonic part of the Laval nozzle and is then accelerated to supersonic flow speed or the wake starts shortly after the nozzle throat and is then further accelerated depending on the injector geometry. The four different injector geometries with subsonic injection, subsequently called injector 1 to 4, were investigated in a previous study and the results are shown in [14] in detail. In this study the trailing edge of the injectors was extended so that it lay in the supersonic part of the Laval nozzle. These injectors with supersonic injection are called injector 5 to 8 subsequently. Here, the results of the experimental investigation with supersonic injection will be shown and compared to the ones with subsonic injection.

The wake structure was investigated by applying laser-induced fluorescence (LIF) imaging with a toluene-seeded nitrogen flow as a replacement for the precursor flow. The fluorescence properties of toluene are well characterized [15, 16, 17, 18] and this component is therefore used for the investigation of the spatial distribution of the precursor substitute.

2. Experimental Facility and Diagnostics

All experiments shown in this study were conducted at the supersonic test facility of the Institute of Aerospace Thermodynamics (ITLR) at the University of Stuttgart (see Fig. 1). A detailed description of the test facility is shown in [19]. Briefly, it contained a screw compressor, an air dryer, a two-stage electrical heater and an exchangeable test section, here the optically accessible flow duct. The continuously operating screw compressor delivered air at a maximum of 10 bar with a maximum flow rate of 1.45 kg/s. The dried and compressed air can be heated up to 1500 K. The total pressure and the total temperature of the air stream were measured at the exit of the second heater with uncertainties of ±5 kPa and ±2 %, respectively. The mass flow rate of the air stream was measured with a vortex flow meter in combination with temperature and pressure instruments.

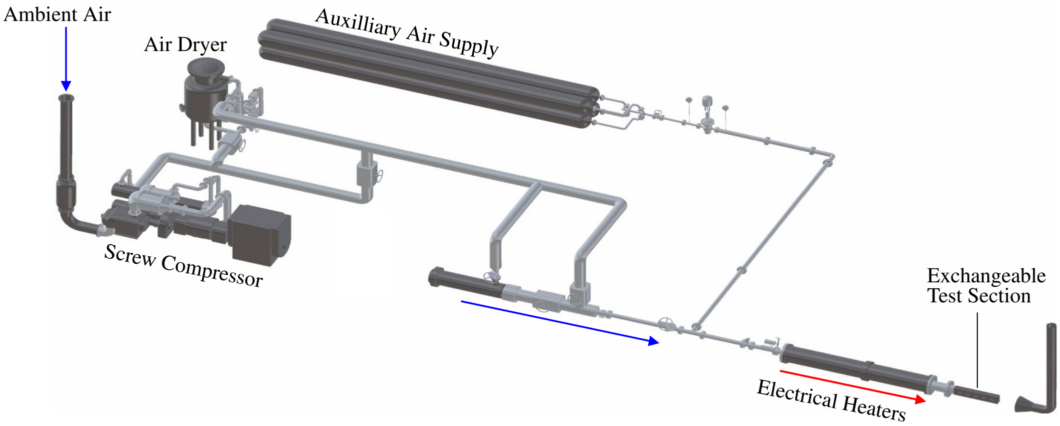

Figure 1: Schematic of the supersonic test facility at the ITLR

In all following descriptions, the x-coordinate represents the streamwise direction, the y-axis defines the spanwise direction, and the z-axis is located normal to the main flow direction. The origin of the coordinate system is located in the center of the nozzle throat.

2.1 Test section

The air flow through a rectangular Laval nozzle with a width of 40 mm, a total length of 800 mm, and a nozzle throat height of 20 mm was observed. The duct was made from aluminum and contained two side plates, one top plate and one bottom plate (see Fig. 2). To feed a laser sheet for LIF measurements into the duct on the top and bottom walls laser slots, made of fused silica, were integrated and followed the shape of the Laval nozzle. Flat quartz windows were attached from both sides for optical access in order to observe the mixing from the injector trailing edge. At the top wall of the duct 29 pressure tapping points each with a diameter of 1 mm were installed to measure the wall static pressure. Long pressure tubes connected these holes to pressure sensors (Scanivalve Corp. DSA3016, uncertainty ≤ 0.05% FS) each having 16 channels. The measurement frequency per tube was 200 Hz. Thermocouples were integrated in the duct flow and in the injector flow, having an accuracy of ±1.1 K.

In a previous study four injectors were mounted that have their trailing edge shortly before the nozzle throat (see Fig. 3) at x = -42.1 mm [20, 14]. In this study the trailing edge of the subsonic injectors was extended into the supersonic region of the Laval nozzle and lay at $x = 10.0\,\text{mm}$ (see Fig. 3 and Fig. 4a). Thus, the ambient air Mach number at the injector trailing edge was about 0.79 for subsonic injection and 1.15 for supersonic injection. In all experiments with subsonic injection the ambient air flow had a total pressure of 2 bar. To keep the mass flow rate of 0.330 kg/s through the duct identical to that with subsonic injection, the total pressure was increased for experiments with supersonic injection, where the nozzle throat was reduced by the injector. Thus, the air flow had a total pressure of 2.67 bar. The total temperature was 380 K in all experiments. The Reynolds number based on the nozzle throat was about $Re \approx 5.8 \cdot 10^5$ for subsonic injection and about $Re \approx 4.7 \cdot 10^5$ for supersonic injection.

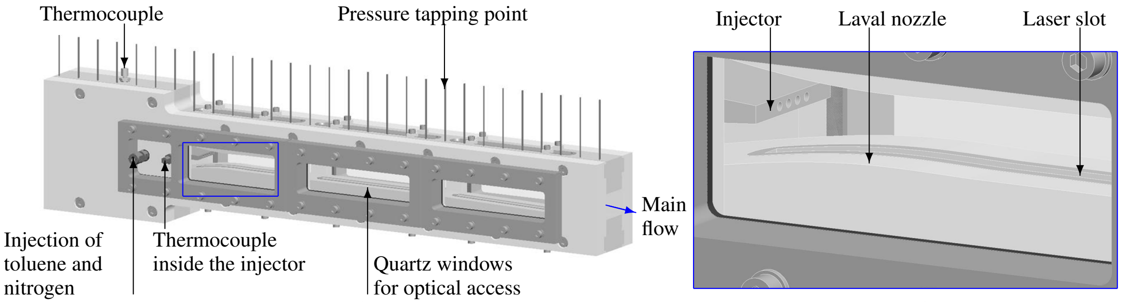

(a) Complete flow duct

(b) Detailed view of the Laval nozzle

Figure 2: Flow duct for mixing experiments with injector 1 for subsonic injection mounted

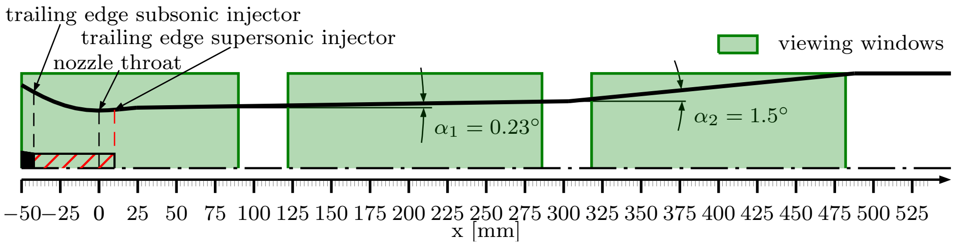

Figure 3: Duct contour including the injector trailing edges, the nozzle throat and the position of all viewing windows

The investigated types of injectors for the supersonic injection were identical to the subsonic injection but with an extended trailing edge. This is shown in Fig. 4a where additional red lines mark the injector trailing edge in case of subsonic injection. Injector 1 to 4 represent the injectors with subsonic injection and the geometries can be found in [14]. Injector 5 to 8 represent the injectors with supersonic injection. An overview of all injectors is given in Tab. 1.

Table 1: Sketch of the different injectors for subsonic and supersonic injection

Injectors with subsonic injection		**Injectors with supersonic injection**	
Injector 1	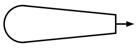	Injector 5	
Injector 2	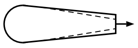	Injector 6	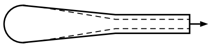
Injector 3	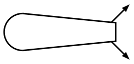	Injector 7	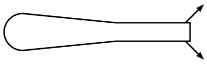
Injector 4	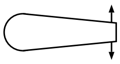	Injector 8	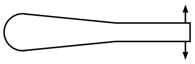

Injector 5 had four injecting holes each with a diameter of 2.5 mm (see Fig. 4a) so that the injector flow was parallel to the ambient air flow direction. In contrast, the injector flow direction in case of injector 7 and injector 8 was at an angle of 45° (see Fig. 4c) and 90° (see Fig. 4d) to the normal flow direction, respectively. Injector 6 had the same injector hole positions as injector 1 but was designed with ramps on the upper and lower surfaces of the trailing edge (see Fig. 4b).

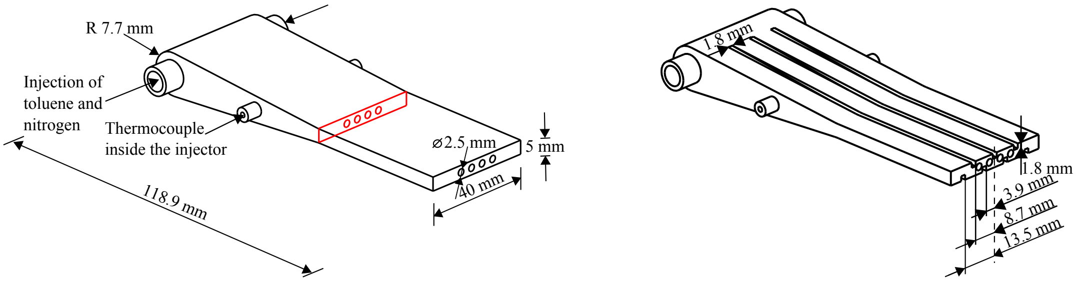

(a) Injector 5 (red lines indicate the trailing edge of injector 1 for subsonic injection)

(b) Injector 6

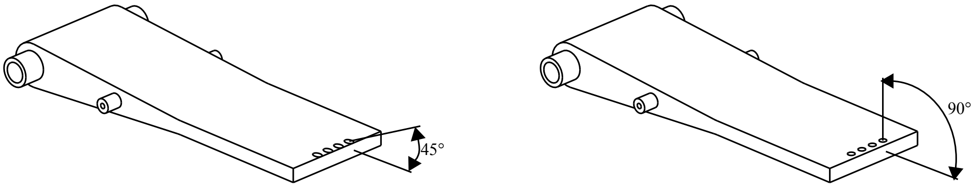

(c) Injector 7

(d) Injector 8

Figure 4: Investigated injector geometries with supersonic injection

A gaseous toluene-seeded nitrogen flow was used as a substitute for the precursor flow and was mixed into the duct air flow through the eight different injector geometries. The injector flow was provided by a Controlled Evaporator Mixing (CEM) system (Bronkhorst). A controlled amount of toluene was introduced into the CEM from a reservoir. Nitrogen entered the CEM as well and was mixed with the evaporated toluene. A magnetic valve and a mass flow meter controlled and measured the mass flow rate of the injectant with an uncertainty of $\leq \pm 5\%$. The seeded flow consisted of 0.14 g/s toluene and 0.42 g/s nitrogen. Thus, the injector massflow rate was 0.56 g/s and the injected mass flow was about $\dot{m} \approx 0.17\%$ of the ambient air flow. These mass flows were kept constant throughout all experiments with all injectors. The Schmidt number was calculated directly at the injector trailing edge with the temperature dependent diffusion coefficient for gases using the Chapman-Engskog theory and resulted in $Sc \approx 0.905$ in case of subsonic injection and in $Sc \approx 0.901$ in case of supersonic injection. Thus, the injector flow diffuses practically at the same rate as momentum. The total pressure of the injector flow was 6 bar and the total temperature was 380 K. The gas was introduced to the injector from both sides by a heated tube to prevent the mixture from condensing. Furthermore, it was important to take into account that the supersonic flow reached sub-zero temperatures at the end of the duct and thus, condensation of toluene needed to be considered. However, calculations of the vapour pressure of toluene showed that condensation did not take place in the operating conditions, see [21] for details.

2.2 LIF setup

The flow structures were visualized applying non-intrusive LIF imaging. A krypton fluoride excimer laser (Lambda Physik, LPX 120) with a beam at 248 nm wavelength (20 ns pulse width, broadband output) was used to excite the injector flow. The formed laser light sheet was 0.5 mm thick and 25 mm wide and passed the flow duct from the top to the bottom through laser slots parallel to the main flow in the center of the flow duct (see Fig. 5). Two hundred instantaneous LIF images were taken for each measurement position all along the test section, capturing the peak fluorescence signals ($\lambda = 280 \pm 14$ nm) at 90° to the flow. To detect the fluorescence an intensified charge-coupled device (ICCD) camera with 200 ns exposure time (LaVision, Imager Intense) was located perpendicular to the laser sheet plane. Measurements were carried out with an 8 Hz repetition rate. All optical equipment was installed on a moveable optical table that was used to shift the entire LIF setup including laser, detector and sheet-forming optics relative to the duct.

3. Results and Discussion

The measured wall static pressure shown in Fig. 6 represents an averaged value because the pressure transducers used in the experiments reacted very slowly. The diagram shows the normalized wall static pressure for injectors with

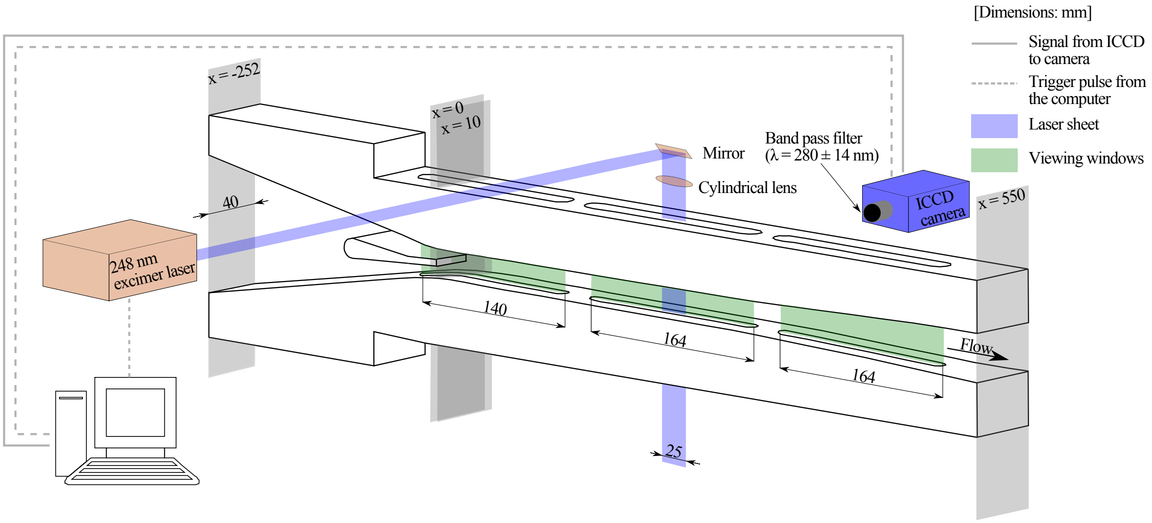

Figure 5: Schematic of the LIF setup and the flow duct dimensions

subsonic injection (black curve, $p_0 = 2\,\mathrm{bar}$) and with supersonic injection (red curve, $p_0 = 2.67\,\mathrm{bar}$) as a function of the distance to the nozzle. In both cases, subsonic and supersonic injection, the pressure decreased until $x \approx 35\,\mathrm{mm}$, which indicated that the flow was accelerated to supersonic flow speed in the Laval nozzle. Further downstream the duct, the opening angle was smaller than the growth rate of the wake between $x \approx 35 - 120\,\mathrm{mm}$ for subsonic injection and between $x \approx 35 - 60\,\mathrm{mm}$ for supersonic injection. This led to a restriction of the ambient air flow and thus to a small increase in the wall static pressure distribution. The pressure in the middle section of the duct was almost constant because of a very small opening angle of the duct of 0.23°. Further downstream the flow was again accelerated by an increasing cross section with an angle of 1.5°. Due to overexpansion of the supersonic flow at the duct outlet a shock train decelerated the flow.

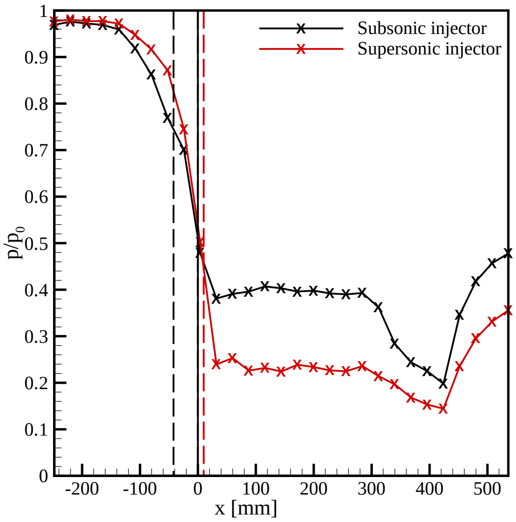

Figure 6: Measured wall static pressure as a function of the distance to the nozzle. The injector trailing edge for subsonic injection lay at x = -42.1 mm, for supersonic injection at x = 10 mm and the nozzle throat at x = 0 mm.

3.1 Instantaneous LIF images

The recorded raw LIF images were post-processed to correct for laser light sheet inhomogeneities and background signal. The instantaneous LIF images in case of supersonic injection are shown for the first viewing window in Fig. 7.

The instantaneous LIF images on all positions and a comparison with the LIF images in case of subsonic injection are shown in detail in [22], so just a brief overview will be given here.

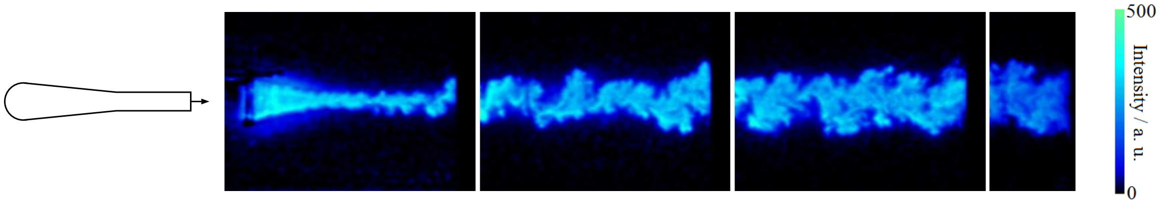

(a) Injector 5

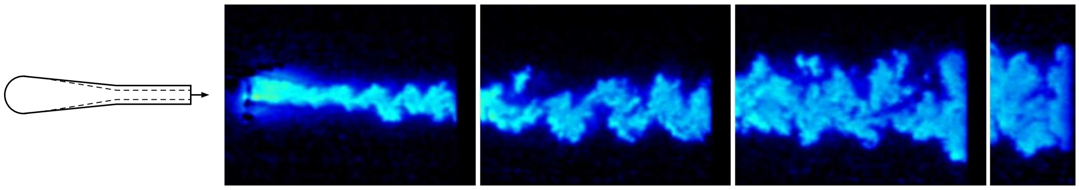

(b) Injector 6

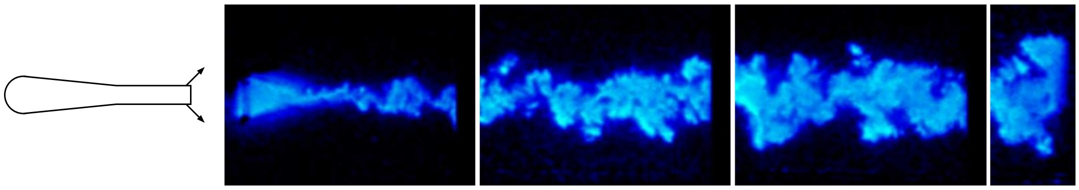

(c) Injector 7

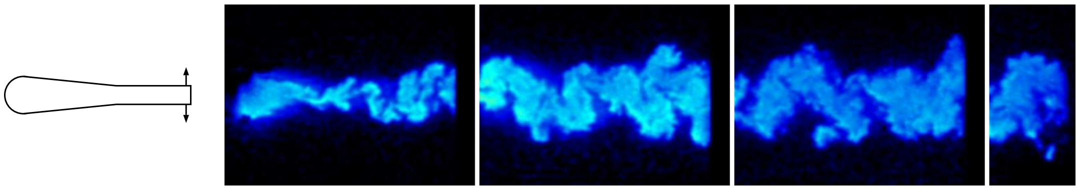

(d) Injector 8

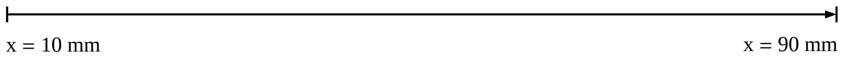

Figure 7: Instantaneous toluene-LIF images using different injector geometries with supersonic injection

It can be seen from the instantaneous LIF images that the injector flow was pushed to the centerline shortly after the trailing edge in case of all injector geometries with supersonic injection. This was due to the expansion fan and the recompression waves located at the injector trailing edge (see [22] for the Schlieren images). The smallest cross section on the injector flow was identical with the "neck" formed by the recompression ([23]). Further downstream the flow spread out and mixed with the ambient air. The flow structures in the far field of the wake for the injectors with supersonic injection look similar to the ones produced by the ramp injector with subsonic injection (injector 2). The counter-rotating vortical structures typical for injector 1 did not appear, but a zig-zag-like pattern can be observed. Furthermore, it can be seen that the toluene-LIF intensity in the recompression region is higher for injector 5 and 6 compared to injector 7 and 8. This is due to the fact that the injector flow was at an angle to the ambient air flow direction and therefore wasn't mixed directly into the recirculation zone at the injector trailing edge. The mixing structures in case of injector 6 differed from the other injectors behind the trailing edge, where the injector flow was angled. This was due to the ramps on the upper and lower surface of the injector.

3.2 Averaged LIF measurements

The instantaneous LIF images showed the flow structures behind the injector trailing edge in detail. But to get more information about the wake, averaged LIF images were needed. For this all two hundred instantaneous images were averaged and corrected for background signal and lasersheet energy variations. Averaged LIF images are shown in Fig. 8 for injector 5 and 6 exemplarily. In both cases it can be seen that the injector flow was pushed to the duct centerline due to recompression waves and the "neck" is formed at about $x = 20$ mm. This flow behaviour was less distinctive for injector 6. Additionally, the angled injector flow in case of injector 6 can be seen till about $x = 60$ mm. Downstream the "neck" the injector flow was spread out and mixed with the ambient air flow. From the averaged images it can be seen, that the injector flow in case of injector 6 spread out more. This was in contrast to the injectors with subsonic injection, where the injector flow in case of injector 2 was not spread out as much as in case of injector 1.

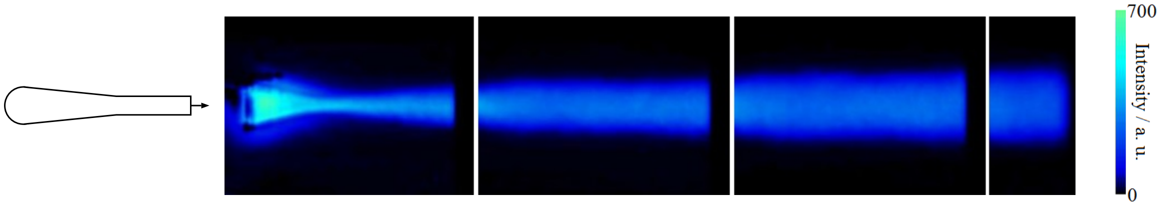

(a) Injector 5

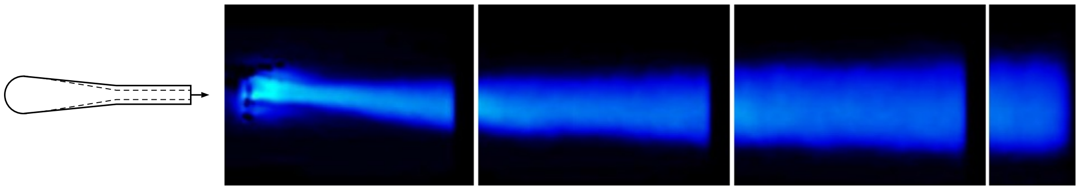

(b) Injector 6

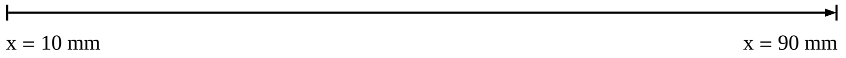

Figure 8: Averaged toluene-LIF images for injector 5 and 6 in the first duct window

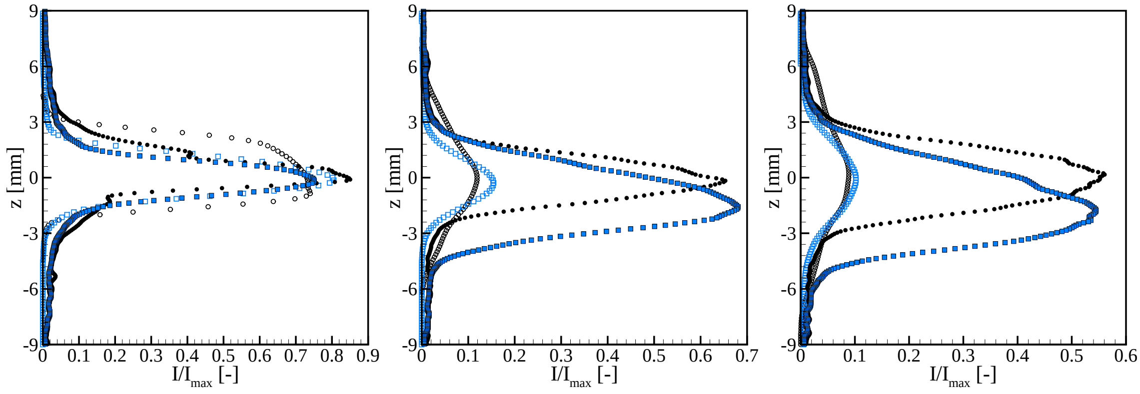

(a) d = 2.1 mm (b) d = 18.1 mm (c) d = 42.1 mm

Figure 9: Normalized toluene-LIF intensity profiles at different distances downstream of the injector trailing edge d; ○: injector 1, □: injector 2, ●: injector 5, ■: injector 6

From the averaged LIF images intensity profiles were extracted and normalized to the maximum intensity I_{max} directly at the injector trailing edge. The profiles are shown in Fig. 9 for some locations downstream of the injector trailing edge for injector 5 and 6 exemplarily and compared to injector 1 and 2. Figure 9a shows the normalized toluene-LIF intensity profiles shortly after the injector trailing edge at $d = 2.1$ mm, where d denotes the distance to the trailing edge. It can be seen that the maximum is more or less in the same range for all injectors but the injector flow in case of injector 1 already spread out more compared to the other injectors because of the typical counter-rotating vortical structures, which can be also seen in Fig. 9b and 9c. Further downstream the normalized intensity is much higher in case of supersonic injection. At $d = 18.1$ mm it is in the range of 0.65 for the supersonic injection and in the range of 0.13 for the subsonic injection for example. Also the angled injector flow in case of injector 6 can be seen in the intensity profiles in Fig. 9b and 9c. The sign of the offset in z-direction changed if injector 6 was mounted mirrored through the xy-plane.

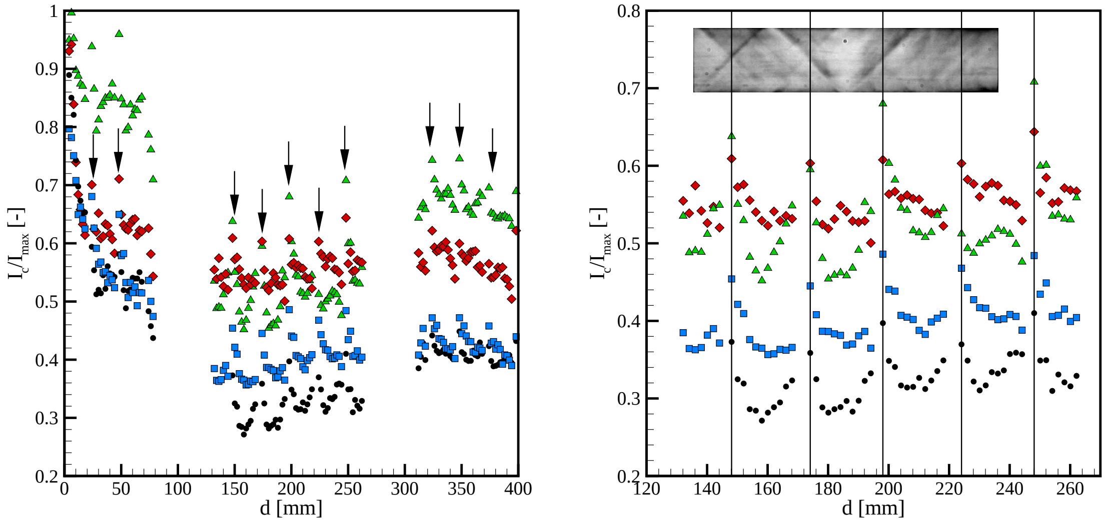

(a)

(b)

Figure 10: Maximum toluene-LIF intensity plots; ●: injector 5, ■: injector 6, ◆: injector 7, ▲: injector 8

Figure 10 shows the local maximum intensity normalized by the maximum intensity directly at the injector trailing edge plotted against the distance to the trailing edge d. The maximum intensity along all viewing windows for all injectors with supersonic injection is shown in Fig. 10a. An asymptotic behaviour can be seen for all injectors. The intensity decreased until the end of the first viewing window quickly. In the second and third window the normalized maximum intensity tended to a nearly constant value. Additionally, some peaks were observed for all injectors with supersonic injection. This is shown in an enlarged plot for the second viewing window in Fig. 10b. A comparison with the Schlieren images showed that these peaks appear at the intersection points of the reflected shock waves. The Schlieren image of injector 6 is therefore plotted in Fig. 10b too. All Schlieren images and a comparison of the maximum intensity for subsonic and supersonic injection can be found in [22].

To quantify the self-preserving state of the wake a Gaussian fit was applied to all intensity profiles over the central portion of the flow in steps of 2 mm from the recompression "neck" up to 78 mm from the trailing edge. From this fitting the local centerline position $z_c(x)$, the local maximum intensity $I_c(x)$ and the local half-width $\delta_{1/2}(x)$ of each downstream intensity profile were obtained. Figure 11 shows all local mean intensity profiles obtained from the averaged LIF images. All profiles were normalized by the local maximum value $I_c(x)$. In the lateral direction the difference between z and the maximum location z_c normalized by the local half-width $\delta_{1/2}(x)$ is plotted. The figures show that the profiles were self-similar for all four injectors with supersonic injection and the normalized profiles were independent of the shape of the wake generator. The highest deviations were observed for injector 8. Furthermore, the shape of the intensity profiles were compared with the incompressible wake profile shape reported in [5] for the velocity deficit profile. The normalized toluene intensity profiles were in good agreement with the incompressible profile shape. That demonstrated that the self-similarity of the profiles also exists in the investigated compressible flow with changing pressure gradient and supersonic injection. This behaviour was proved also with subsonic injection and self-similarity was observed as well [14]. The incompressible profile is also compared with supersonic wakes at Mach 2 and 3 in [9] and a good agreement is shown as well.

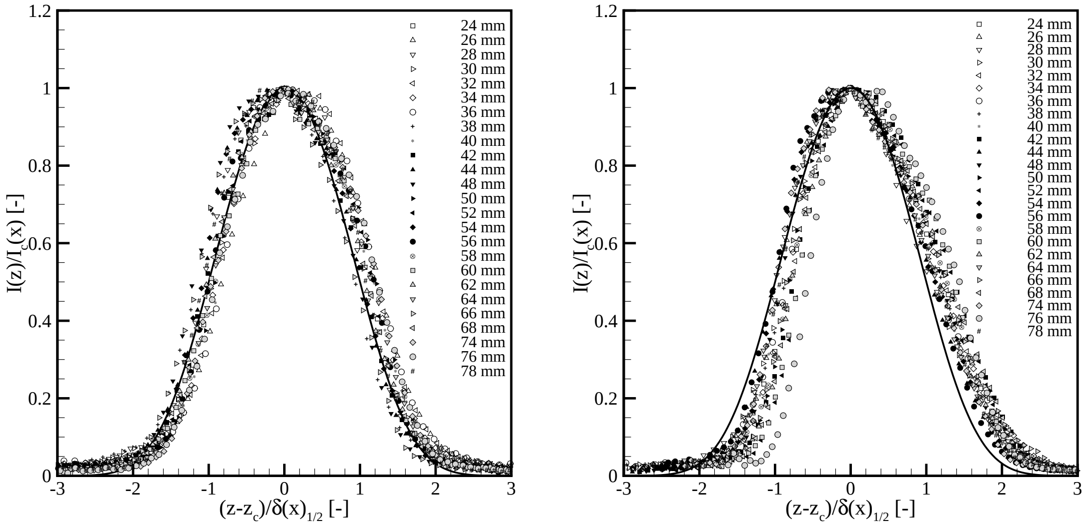

(a) Injector 5 (b) Injector 6

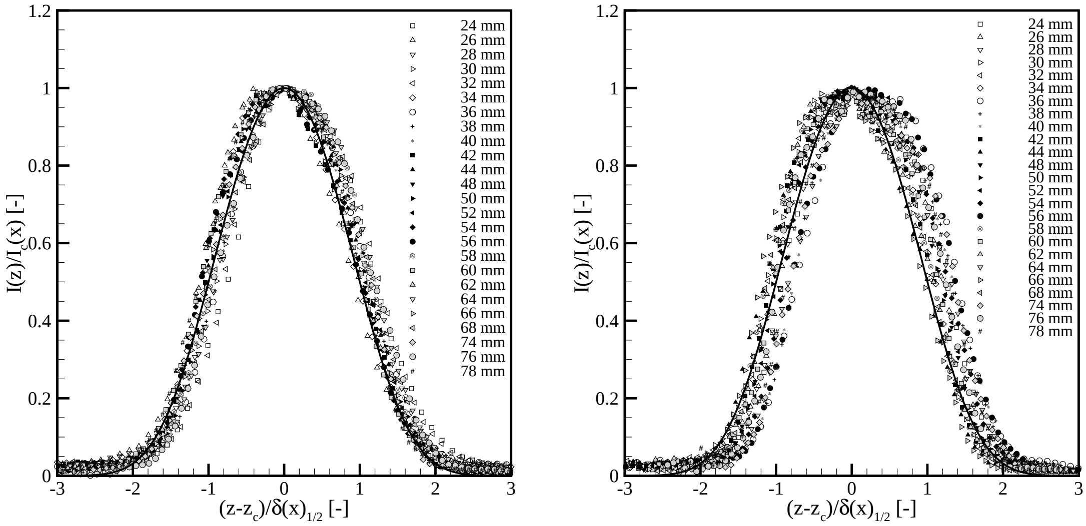

(c) Injector 7 (d) Injector 8

Figure 11: Similarity of the toluene-LIF intensity profiles at various downstream locations for all investigated injectors with supersonic injection. The solid line indicates the incompressible wake profile shape reported in [5] for the velocity deficit profile.

3.3 Outer length scale of the wake

From the LIF intensity profiles and the Gaussian fit, the half-width $\delta_{1/2}(x)$ of each downstream intensity profile was calculated. Various studies [5, 23] show that the half-width of the wake is directly proportional to the root mean square of the distance to the injector trailing edge ($\delta_{1/2} \sim d^{1/2}$) as predicted by the equation of motion and the momentum integral constraint.

Figure 12a shows the squared half-width at different axial positions for the first and second viewing window for all injectors with supersonic injection. Furthermore, the method of least squares was applied to the experimental results and the best-fit line is plotted for each injector in the same diagramm. It can be seen from the best-fit lines that the growing rate of the wake follows the 1/2-power-law in accordance to the theory from the recompression "neck" to the end of the second window, beside some deviations in case of injector 6 in the second window and in case of injector 8 at the end of the second window. It can be seen that the growing rate of the wake for injector 7 and 8 did not show big variations and they were larger than for injector 5, just like observed for injector 1, 3 and 4. In contrast to the injectors with subsonic injection, where injector 2 had the lowest growing rate, the growing rate of injector 6 was the largest one. Figure 12b shows the squared half-width for all injectors with supersonic injection until a distance of $d = 50\,\text{mm}$ from the injector trailing edge. Here the recompression "neck" can be seen clearly at about $d \approx 8\,\text{mm}$ behind the trailing edge for injector 5 and 6 and at about $d \approx 6\,\text{mm}$ behind the trailing edge for injector 7 and 8. In this near-field wake the growing rate did not follow the 1/2-power-law and consequently the intensity profiles did not show self-similar behaviour in this region.

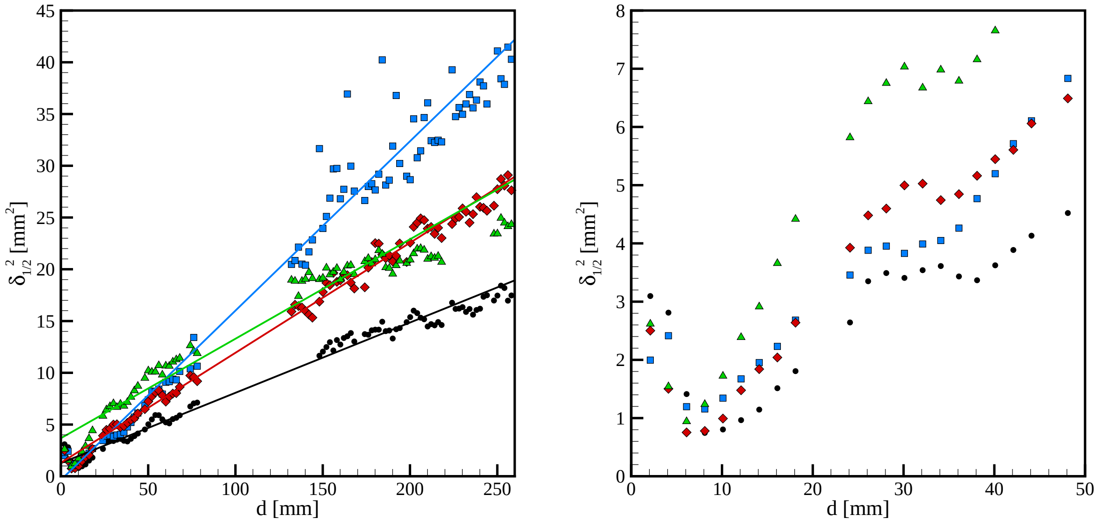

(a)

(b)

Figure 12: Squared half-width of the growing wake and best-fit lines calculated with the method of least squares; ●: injector 5, ■: injector 6, ◆: injector 7, ▲: injector 8

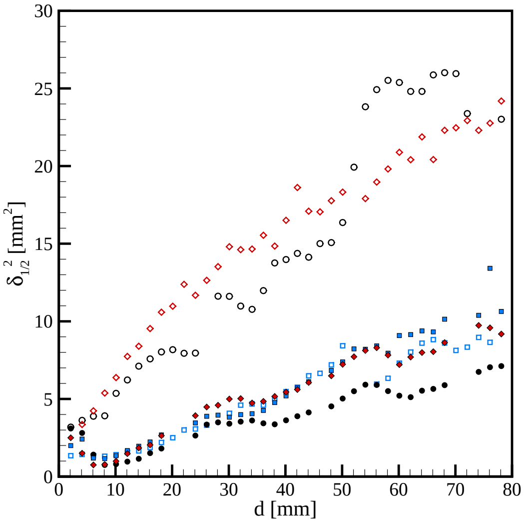

Figure 13: Squared half-width for subsonic and supersonic injection for the first viewing window; ○: injector 1, □: injector 2, ◇: injector 3, ●: injector 5, ■: injector 6, ◆: injector 7

In Fig. 13 a comparison of the squared half-width of the growing wake between injector 1, 2 and 3 with subsonic injection and injector 5, 6 and 7 with supersonic injection is shown until a distance of $d = 80\,\text{mm}$ to the injector trailing edge. The squared half-width for injector 4 and 8 are not shown in this diagram because they are very similar to injector 3 and 7, respectively. It can be seen that the growing rate for injectors with supersonic injection were all in the same range as injector 2, the ramp injector with subsonic injection.

4. Conclusions

The mixing processes in a compressible accelerated nozzle flow with subsonic and supersonic injection were investigated experimentally and the results were compared. The flow structures were visualized applying LIF imaging and the instantaneous images showed a zig-zag-like flow structure in case of all injectors with supersonic injection and no counter-rotating vortical structures that were observed for injectors with subsonic injection. The averaged images showed that the flow was pushed to the centerline shortly behind the trailing edge due to recompression waves and a "neck" was formed. Intensity plots on different downstream locations showed that the maximum intensity at the duct centerline was much higher in case of supersonic injection. The maximum toluene-LIF intensity plot showed an asymptotic behaviour and intensity peaks that were equal to the intersection points of the reflected shock waves. Furthermore, the toluene intensity profiles were shown for all injectors with supersonic injection and they were independent of the shape of the wake generator and remained invariant on different downstream locations. A comparison with the wake profile shape reported for the velocity deficit profile in incompressible wakes showed good agreement. Additionally, the half-width $\delta_{1/2}(x)$ of the wake was directly proportional to the mean root square of the distance to the trailing edge and thus followed the 1/2-power-law behind the recompression "neck". Finally, it was observed that the growing rate for injectors with supersonic injection were in the same range as injector 2, the ramp injector with subsonic injection.

5. Acknowledgements

The authors gratefully acknowledge funding by the Deutsche Forschungsgemeinschaft, DFG.

References

[1] Dannehl, M., A. Maisels, W. Leibold, H. Olivier, A. Grzona, A. Weiß, A. Gülhan, T. Gawehn, G. H. Schnerr, N. Al-Hasan, A. Abdali, M.Y. Luong, H. Wiggers, C. Schulz, B. Weigand, J. Chun, W. Schröder, M. Meinke, T. Winnemöller, H. Nirschl, V. Goertz, K. Schaber, and T. Rakel. 2007. Nanoparticle synthesis by gas-dynamically induced heating and quenching. *European Aerosol Conference*.

[2] Grzona, A., A. Weiß, H. Olivier, T. Gawehn, A. Gülhan, N. Al-Hasan, G.H. Schnerr, A. Abdali, M. Luong, H. Wiggers, C. Schulz, J. Chun, B. Weigand, T. Winnemöller, W. Schröder, T. Rakel, K. Schaber, V. Goertz, H. Nirschl, A. Maisels, W. Leibold, and M. Dannehl. 2007. Gas-phase synthesis of non-agglomerated nanoparticles by fast gasdynamic heating and cooling. *26th International Symposium on Shock Waves*.

[3] Brown, G. L., and A. Roshko. 1974. On density effects and large structure in turbulent mixing layers. *Journal of Fluid Mechanics*. 64: 775–816.

[4] Waitz, I. A., Y. J. Qiu, T. A. Manning, A. K. S. Fung, J. K. Elliot, J. M. Kerwin, J. K. Krasnodebski, M. N. Sullivan, D. E. Tew, E. M. Greitzer, F. E. Marble, C. S. Tan, and T. G. Tillmann. 1997. Enhanced mixing with streamwise vorticity. *Progress in Aerospace Sciences*. 33: 323–351.

[5] Wygnanski, I., F. Champagne, and B. Marasli. 1986. On the large-scale structures in two-dimensional, small-deficit, turbulent wakes. *Journal of Fluid Mechanics*. 168: 31–71.

[6] Barre, S., C. Quine, and J. P. Dussauge. 1994. Compressibility effects on the structure of supersonic mixing layers: experimental results. *Journal of Fluid Mechanics*. 259: 47–78.

[7] Papamoschou, D., and A. Roshko. 1988. The compressible turbulent shear layer: an experimental study. *Journal of Fluid Mechanics*. 197: 453–477.

[8] Gutmark, E. J., K. C. Schadow, and K. H. Yu. 1995. Mixing enhancement in supersonic free shear flows. *Annual Review of Fluid Mechanics*. 27: 375–417.

[9] Nakagawa, M., and W. J. A. Dahm. 2006. Scaling properties and wave interactions in confined supersonic turbulent bluff-body wakes. *AIAA Journal*. 44: 1299–1309.

[10] Drummond, J. P., D. S. Diskin, and A. D. Cutler. 2002. Fuel-air mixing and combustion in scramjets. *AIAA 2002-3878*.

[11] Vellaramkalayil, J., T. Scheuermann, and J. von Wolfersdorf. 2009. Numerical and experimental investigation of a two-staged supersonic combustion chamber. *16th AIAA/DLR/DGLR International Space Planes and Hypersonic Systems and Technologies Conference*.

[12] Gerlinger, P., P. Kasal, F. Schneider, J. von Wolfersdorf, B. Weigand, and M. Aigner. 2005. Experimental and numerical investigation of lobed strut injectors for supersonic combustion. *John Wiley & Sons*. Chapter 5.5: 365–382.

[13] Gaston, M. J., N. R. Mudford, and F. Houwing. 1998. A comparison of two hypermixing fuel injectors in a supersonic combustor. *AIAA 98-0964*.

[14] Wohler A., K. Mohri, C. Schulz, and B. Weigand. Mixing processes in a compressible accelerated nozzle flow with blunt-body wakes. *AIAA Journal*. Submitted for publication.

[15] Koban, W., J. D. Koch, R. K. Hanson, and C. Schulz. 2005. Toluene LIF at elevated temperatures: Implications for fuel/air ratio measurements. *Appl. Phys. B*. 40: 147–150.

[16] Koban, W., J. D. Koch, R. K. Hanson, and C. Schulz. 2005. Oxygen quenching of toluene fluorescence at elevated temperatures. *Appl. Phys. B*. 80: 777–784.

[17] Koban, W., J. D. Koch, R. K. Hanson, and C. Schulz. 2004. Absorption and fluorescence of toluene vapor at elevated temperatures. *Phys. Chem. Chem. Phys.*. 6: 2940–2945.

[18] Mohri, K., M. Luong, G. Vanhove, T. Dreier, and C. Schulz. 2011. Imaging of the oxygen distribution in an isothermal turbulent free jet using two-color toluene LIF imaging. *Appl. Phys. B.*. 103: 707–715.

[19] Kasal, P., P. Gerlinger, R. Walter, J. von Wolfersdorf, and B. Weigand. 2002. Supersonic combustion: fundamental investigations of aerothermodynamic key problems. *11th AIAA/AAAF International Conference*.

[20] Wohler, A., K. Mohri, C. Schulz, and B. Weigand. 2011. Flow structures in subsonic-to-supersonic mixing processes using different injector geometries. *4th European Conference for Aeronautics and Space Sciences (EUCASS)*.

[21] Mohri, K., A. Wohler, B. Weigand, and C. Schulz. 2011. Toluene laser-induced fluorescence (LIF) imaging of supersonic flow within a diverging duct. *28th International Symposium on Shock Waves*.

[22] Mohri, K., A. Wohler, B. Weigand, and C. Schulz. 2013. Toluene laser-induced fluorescence (LIF) imaging of supersonic flow within a diverging duct with injectors in the supersonic region. *29th International Symposium on Shock Waves*.

[23] Nakagawa, M., and W. J. A. Dahm. 2005. Virtual origin of incompressible and supersonic turbulent bluff-body wakes. *AIAA Journal*. 43: 697–700.